

Spatial and Polarization Division Multiplexing Harnessing On-Chip Optical Beam Forming

González-Andrade, David; Le Roux, Xavier; Aubin, Guy; Amar, Farah; Nguyen, Thi Hao Nhi; Nuño Ruano, Paula; Dinh, Thi Thuy Duong; Oser, Dorian; Pérez-Galacho, Diego; More Authors

DOI

[10.1002/lpor.202300298](https://doi.org/10.1002/lpor.202300298)

Publication date

2023

Document Version

Final published version

Published in

Laser and Photonics Reviews

Citation (APA)

González-Andrade, D., Le Roux, X., Aubin, G., Amar, F., Nguyen, T. H. N., Nuño Ruano, P., Dinh, T. T. D., Oser, D., Pérez-Galacho, D., & More Authors (2023). Spatial and Polarization Division Multiplexing Harnessing On-Chip Optical Beam Forming. *Laser and Photonics Reviews*, 17(11). <https://doi.org/10.1002/lpor.202300298>

Important note

To cite this publication, please use the final published version (if applicable). Please check the document version above.

Copyright

Other than for strictly personal use, it is not permitted to download, forward or distribute the text or part of it, without the consent of the author(s) and/or copyright holder(s), unless the work is under an open content license such as Creative Commons.

Takedown policy

Please contact us and provide details if you believe this document breaches copyrights. We will remove access to the work immediately and investigate your claim.

Spatial and Polarization Division Multiplexing Harnessing On-Chip Optical Beam Forming

David González-Andrade,* Xavier Le Roux, Guy Aubin, Farah Amar, Thi Hao Nhi Nguyen, Paula Nuño Ruano, Thi Thuy Duong Dinh, Dorian Oser, Diego Pérez-Galacho, Eric Cassan, Delphine Marris-Morini, Laurent Vivien, and Carlos Alonso-Ramos


On-chip spatial and polarization multiplexing has emerged as a powerful strategy to boost the data transmission capacity of integrated optical transceivers. State-of-the-art multiplexers require accurate control of the relative phase or the spatial distribution among different guided optical modes, seriously compromising the optical transmission bandwidth and performance of the devices. To overcome this limitation, a new approach based on the coupling between guided modes in integrated waveguides and optical beams free-propagating on the chip plane is proposed. The engineering of the evanescent coupling between the guided modes and free-propagating beams allows spatial and polarization multiplexing with state-of-the-art performance. A two-polarization multiplexed link and a three-mode multiplexed link using standard 220-nm-thick silicon-on-insulator technology have been developed. The two-polarization link shows a measured -35 dB crosstalk bandwidth of 180 nm, while the three-mode link exhibits a -20 dB crosstalk bandwidth of 195 nm. These links are used to demonstrate error-free operation (bit-error-rate $<10^{-9}$) in multiplexing and demultiplexing of two and three non-return-to-zero signals at 40 Gbps each, with power penalties below 0.08 and 1.5 dB for the two-polarization and three-mode links, respectively. The approach demonstrated for two polarizations and three modes is transferable to future implementation of more complex multiplexing schemes.

1. Introduction

Silicon photonics has been identified as a promising technology to address the traffic bottleneck in data centers and networks facing communication growing.^[1] On-chip optical transceivers fabricated at large volume using microelectronics manufacturing facilities could become instrumental in exploiting optical carriers to boost the data transmission capacity while reducing the power consumption of the transmitted bit per second in communication systems.^[2,3] Current silicon photonics optical transceivers carry different data channels at distinct wavelengths using wavelength-division multiplexing (WDM).^[4] However, as the industry moves forward with the development of next-generation optical networks, other multiplexing schemes will be required to support a higher data capacity per wavelength channel. One promising approach is the use of spatially-distributed modes to encode more data channels at a specific wavelength combining even orthogonal polarization modes as in current systems with low-loss multiplexer.^[5] The manipulation of higher-order modes and polarization state of light on chip

D. González-Andrade, X. Le Roux, G. Aubin, F. Amar, T. H. N. Nguyen, P. Nuño Ruano, T. T. D. Dinh, D. Oser, E. Cassan, D. Marris-Morini, L. Vivien, C. Alonso-Ramos
Centre de Nanosciences et de Nanotechnologies
CNRS
Université Paris-Saclay
Palaiseau 91120, France
E-mail: david.gonzalez-andrade@c2n.upsaclay.fr

D. Oser
QuTech and Kavli Institute of Nanoscience
Delft University of Technology
Delft 2600 GA, The Netherlands
D. Pérez-Galacho
Telecommunication Research Institute (TELMA)
CEI Andalucía TECH
Universidad de Málaga
Málaga 29010, Spain

 The ORCID identification number(s) for the author(s) of this article can be found under <https://doi.org/10.1002/lpor.202300298>

© 2023 The Authors. Laser & Photonics Reviews published by Wiley-VCH GmbH. This is an open access article under the terms of the Creative Commons Attribution License, which permits use, distribution and reproduction in any medium, provided the original work is properly cited.

DOI: 10.1002/lpor.202300298

has thus attracted a significant research interest in the past years for the realization of performant mode and polarization (de)multiplexers.

A myriad of architectures has been proposed to realize mode-division (MDM) and polarization-division multiplexing (PDM). MDM has been demonstrated based on multimode interference (MMI) couplers, asymmetric Y-junctions and directional couplers (DCs), adiabatic tapers, pixelated-meta structures, and sub-wavelength metamaterials.^[6–13] Similarly, multiple devices have been reported for PDM, including MMIs, Mach-Zehnder interferometers (MZIs), diverse types of DCs (i.e., symmetric, asymmetric, tapered, bent, and based on extreme skin-depth), photonic crystals, slot waveguides, and subwavelength and tilted nano-gratings.^[14–27] Despite the great diversity of proposed solutions, crosstalk still remains as one of the main impairments in high-speed optical communications, especially in systems with a high-channel count. An increased crosstalk has a negative impact on the link performance in terms of bit-error-rate (BER) and ultimately results in a power penalty that jeopardizes low power consumption.^[28] Silicon multiplexers handling more than two modes (e.g., 3 spatial modes with the same polarization) yield poor crosstalk values ranging from -19 ^[11] to -9.7 dB.^[7]

Here, we propose a simple yet effective strategy to realize highly efficient mode and polarization (de)multiplexing based on engineered on-chip beam forming. Instead of controlling the phase or field distribution matching between two guided modes, we engineer the evanescent coupling between the modes of a photonic waveguide and free-propagating beams on the chip plane. Coupling between guided modes and on-chip free-propagating beams has been achieved using distributed Bragg deflectors.^[29–33] However, the wavelength-dependent nature of the diffractive coupling seriously limits their use for wideband mode or polarization multiplexers. Conversely, evanescent coupling does not present a strong wavelength dependence, which allowed the demonstration of on-chip beam expanders with a wide bandwidth.^[34–36] In our proposed scheme we engineer the evanescent coupling to make each waveguide mode (or polarization) couple to a different in-plane beam, propagating with a specific angle. As schematically shown in **Figure 1a**, this strategy spatially separates the different waveguide modes, allowing (de)multiplexing. Based on this approach, we experimentally demonstrate a two-polarization link and a three-mode link that allow error-free transmission of multiplexed high-speed data streams. We show transmission of two and three 40 Gbps non-return-to-zero (NRZ) signals, with low or negligible power penalties at a BER of 10^{-9} . To the best of our knowledge, this is the first demonstration of mode and polarization handling enabled by beamforming in an integrated circuit. These devices could be a promising alternative to fixed layout-guided architectures, with excellent potential for the next generation of high-speed and large-capacity on-chip optical interconnects.

2. Mode Division Multiplexing

2.1. Operation Principle

Figure 1a shows the top view of a waveguide evanescently coupled to an adjacent slab. The input waveguide has a width of W and

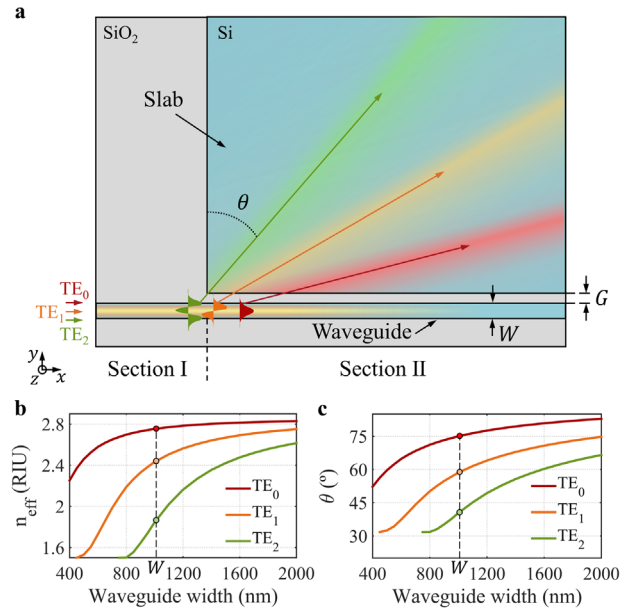


Figure 1. a) Schematic top view of a waveguide evanescently coupled to an adjacent slab. A silicon strip waveguide of width W is placed at a distance G from a silicon slab. Fundamental (red), first-order (orange), and second-order (green) TE modes are injected from the left side of the waveguide and propagate along the x -axis. Each mode is coupled to a vertically-confined (z -axis) beam within the slab with a different propagation angle θ_m . b) Effective index and c) propagation angle within the slab of TE_0 , TE_1 , and TE_2 modes as a function of the waveguide width, calculated for a Si thickness of 220 nm at a wavelength of 1550 nm.

is placed at a distance G from the slab. The waveguide supports a discrete set of guided modes with effective indices of n_{eff}^m , with m being a natural number indicating the mode order. The slab supports a continuum of vertically-confined (z -axis) modes that propagate freely in the xy -plane with a wavenumber given by:

$$\vec{k}_s = k_0 n_s [\sin(\theta) \hat{x} + \cos(\theta) \hat{y}] \quad (1)$$

where n_s is the effective index of the slab, θ is the propagation direction angle of the slab mode with respect to the y -axis, $k_0 = 2\pi/\lambda_0$ is the vacuum wavenumber, and \hat{x} and \hat{y} are the unitary vectors in the x - and y -directions, respectively. Phase-matching between the guided waveguide modes and the slab modes occurs for

$$\sin(\theta_m) = \frac{n_{\text{eff}}^m}{n_s} \quad (2)$$

Note that Equation (2) is analogous to the grating equation when the zero-order harmonic is considered.^[37,38] This zero-order operation obviates the strong wavelength dependence of the propagation angle in distributed Bragg deflectors.^[29–33] The effective indices of the waveguide (n_{eff}^m) and slab (n_s) are wavelength dependent. However, both values are inversely proportional to the wavelength, reducing the wavelength dependence of the ratio n_{eff}^m/n_s . If the separation distance G is sufficiently small, the waveguide mode with effective index n_{eff}^m will evanescently couple to the slab mode propagating with an angle θ_m , satisfying

Equation (2). After a given propagation distance, the different slab modes are spatially separated allowing demultiplexing. Due to reciprocity, the same device can be used to multiplex different slab beams into different waveguide modes.

For the implementation of the proposed architecture, we consider silicon-on-insulator (SOI) with a thickness of the silicon guiding layer of 220 nm. Figure 1b shows the effective indices of the fundamental, first-order, and second-order modes with transverse-electric (TE) calculated as a function of the waveguide width W . Effective indices of the waveguide modes are calculated using a commercial finite difference eigenmode (FDE) solver. The slab index n_s , on the other hand, is calculated by considering a 2D step-index waveguide structure that extends infinitely in the yz -plane and consists of a high refractive index dielectric layer (Si) surrounded by low refractive index material (SiO_2). The thickness of the guiding layer is 220 nm. The modes are calculated using a commercial FDE solver. A sufficiently large simulation window ($>5 \mu\text{m}$) is required in the z -direction to accurately calculate the modes supported by the structure. Using this method, we obtain $n_s = 2.85$ for TE polarization (light polarized along the y -axis) and $n_s = 2.05$ for TM polarization (light polarized along the z -axis) at the wavelength of 1550 nm. Figure 1c shows the propagation angle of the slab modes satisfying Equation (2), considering a slab index $n_s = 2.85$. Differences in propagation angle exceeding 15° can be achieved by properly choosing the waveguide width.

2.2. Design of the Three-Mode Demultiplexer

The proposed three-mode demultiplexer is presented in Figure 2a. The device comprises an input waveguide of width W_I , a coupling region with linearly varying waveguide width and slab separation, and a final section with fixed waveguide width and slab separation of W_E and G_E , respectively. Changing the waveguide width in the coupling region results in a gradual variation of the propagation angle of the slab-propagating beam (see Figure 1c), while the change in the slab gap modifies the coupling strength. These two effects are engineered to focus the slab-propagating beams into a near-Gaussian-shaped profile that is coupled to the fundamental mode of a strip waveguide placed at the focal point. This approach allows coupling each mode of the input waveguide to the fundamental mode of a different output waveguide, thereby performing mode demultiplexing and conversion simultaneously. Note that the approach proposed here can be seamlessly extended to handle a larger number of modes.

The device is designed to maximize the coupling efficiency between each mode of the input waveguide and the corresponding output waveguide while maintaining a low crosstalk. The input waveguide has a width of $W_I = 1 \mu\text{m}$ to support TE_0 , TE_1 , and TE_2 modes in the wavelength range between 1450 and 1650 nm. The dimensions of the coupling region are $G_I = 400 \text{ nm}$, $G_E = 100 \text{ nm}$, $W_E = 200 \text{ nm}$ and $L_T = 35 \mu\text{m}$. These dimensions ensure that all the power in the three input waveguide modes is coupled to slab-propagating beams, simultaneously achieving a near-Gaussian profile for the three slab beams. Further details on the design are provided in Section S1, Supporting Information.

Device performance is assessed using three-dimensional finite-difference time-domain (3D FDTD) simulations. As shown

in Figure 2a, higher-order modes begin to couple to slab beams at early taper positions owing to their weaker modal confinement. The TE_2 (green), TE_1 (orange), and TE_0 (red) modes are completely radiated along the taper as Gaussian-like beams focused on different output points, namely O3, O2, and O1 with respective angles $\theta_2 = 34^\circ$, $\theta_1 = 36^\circ$ and $\theta_0 = 43^\circ$. The position of the focal point for each beam is obtained by searching for the field maximum in the slab region without collecting output waveguides. Figure 2b–d show the normalized magnetic field profile at these focusing points along the axis (ξ_{m+1}), normal to the propagation direction. The radiated fields are fitted to Gaussians with distinct mode field diameters (MFDs), yielding a high overlap integral of 94% for TE_0 input, 87% for TE_1 input, and 92% for TE_2 input. MFDs used for the Gaussians are represented by solid blue curves are 1.9, 3.2, and 4.6 μm . The calculated transmittance to each output is shown in Figure 2e–g when TE_0 , TE_1 , and TE_2 modes are injected into the strip waveguide, respectively. Simulations show insertion losses as low as 0.14 dB at the central wavelength for TE_0 , with a slight increase to 0.65 and 0.69 dB for TE_1 and TE_2 modes, respectively. The degradation of efficiency with wavelength detuning has its origin in chromatic dispersion, which causes a shift of the focal point. Nevertheless, the demultiplexer exhibits a remarkable low crosstalk within a broad bandwidth of 200 nm. Specifically, the attained crosstalk values are better than -41 dB for TE_0 , -40 dB for TE_1 , and -28 dB for TE_2 demultiplexing over the entire simulated bandwidth. The effect of potential fabrication imperfections on device performance is discussed in Section S2, Supporting Information.

2.3. Fabrication and Experimental Characterization of the MDM Link

We implemented a complete MDM link by connecting two-mode (de)multiplexers in a back-to-back configuration through a 20- μm -long multimode waveguide. The link comprises three input and three output single-mode waveguides and a central multimode waveguide. The input multiplexer couples the fundamental mode of each input waveguide to a different mode of the multimode section. The output demultiplexer couples each mode of the multimode waveguide to the fundamental mode of one output waveguide. Focusing grating couplers optimized for TE polarization are used to inject and extract the light from the chip with a fiber array. We included a reference waveguide on the outermost part of the test structure. The device was fabricated using a 220-nm-thick single crystal Si layer of an SOI wafer, with a 3- μm -thick buried oxide layer. The patterns were defined by electron-beam lithography (RAITH EBPG 5000 Plus) and transferred via reactive ion etching (ICP-DRIVE SPTS). Optical and scanning electron microscope (SEM) images were taken prior the deposition of the upper cladding. The sample was then spin-coated with a 1.5- μm -thick PMMA. Figure 3a shows optical images of the MDM link, with zoomed-in SEM images of the taper-slab coupling region and the collecting output waveguides.

Experimental characterization of the link transmittance is shown in Figure 3b–d, when the light is injected through inputs I1, I2, and I3, respectively. The transmittance of each output is obtained by normalizing the measured power at the output ports to

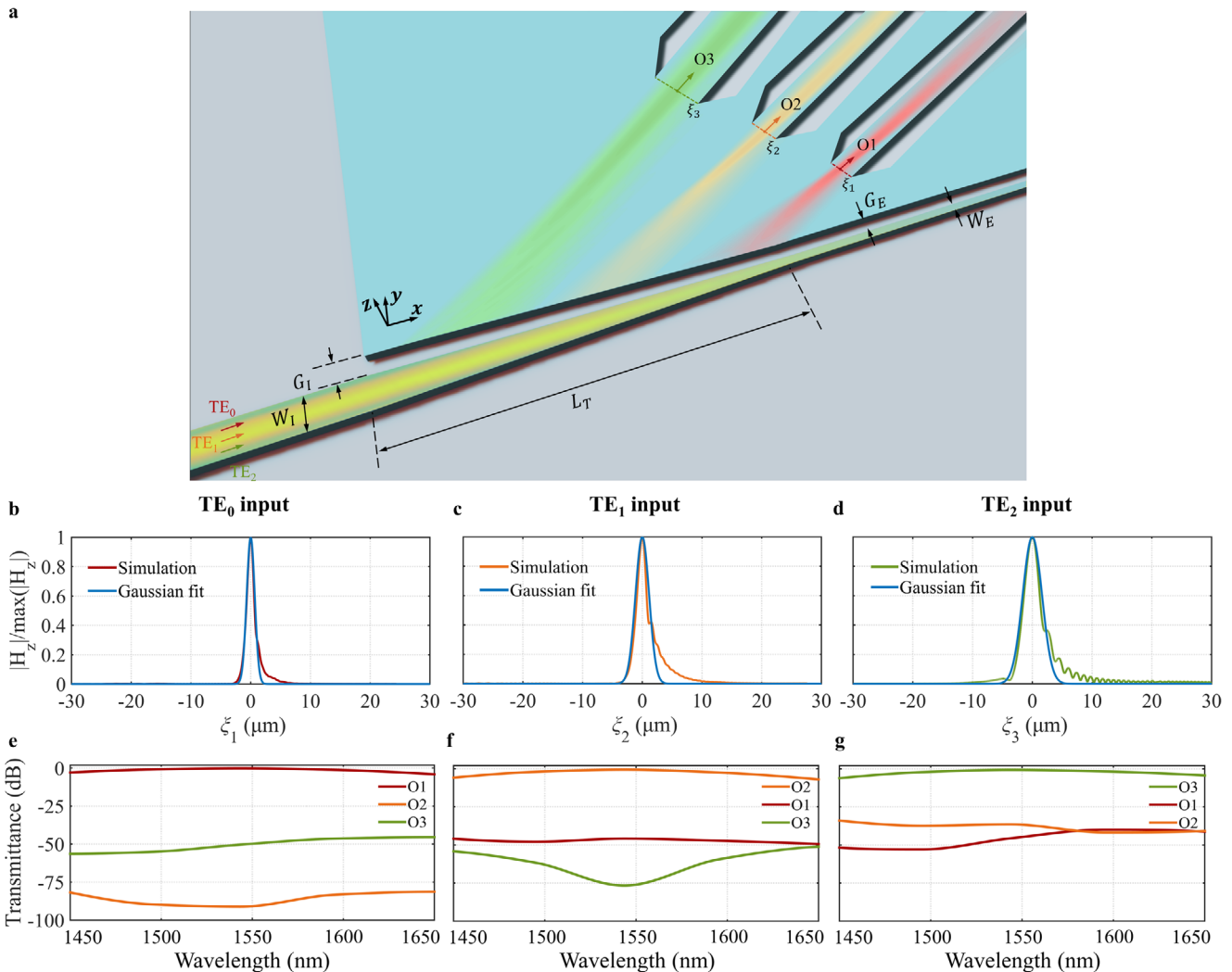


Figure 2. a) Three-dimensional schematic of the proposed three-mode demultiplexer comprising a tapered waveguide and an adjacent slab. The polymethyl methacrylate (PMMA) cladding is not shown for clarity. The simulated electric field distribution in the xy -plane at mid-height of the Si layer is superimposed on the structure when TE₀ (red), TE₁ (orange), and TE₂ (green) are injected at $\lambda_0 = 1550$ nm. Output waveguide apertures are located at the focal points O_{m+1} to collect the free-propagating beams. Normalized magnetic field magnitude $|H_z|$ for b) TE₀, c) TE₁ and d) TE₂ input. Simulated results are obtained from the leaked-field distribution within the slab at the optimum position in the x and y directions for each mode. The field profile is represented along the plane (ξ_{m+1}) , normal to the propagation direction. The simulated transmittance to each of the output as a function of the wavelength when e) TE₀, f) TE₁, and g) TE₂ are launched into the strip nanowire.

the measured power at the reference waveguide output in order to calibrate out the fiber-chip coupling loss. The measured insertion losses are as low as 0.3, 0.9, and 1.7 dB at the transmission peak wavelengths with 1-dB bandwidths of 143, 96, and 84 nm for the TE₀, TE₁, and TE₂ mode channels, respectively. Losses of higher-order modes are larger than fundamental mode losses due to slightly lower overlap with the Gaussian-like profile of the collecting output waveguide modes. On the other hand, measured inter-modal crosstalk is below -31.4, -28.3, and -25.4 dB at the transmission peak wavelengths for TE₀, TE₁, and TE₂ mode channels, respectively.

Additionally, unprecedented crosstalk values reaching -40 dB over a broad bandwidth is observed for TE₀ and TE₂ channels. Considering 1443–1638 nm wavelength range (195 nm bandwidth), the crosstalk is better than -20 dB for all the channels.

Transmission peaks of the three channels are slightly shifted towards shorter wavelengths. We attribute this small discrepancy with simulations to intrinsic fabrication variability.

3. Polarization Division Multiplexing

3.1. Design of the Two-Polarization Demultiplexer

We exploit the proposed approach to demultiplex the two orthogonal TE and transverse-magnetic (TM) polarizations in the waveguide. The proposed two-polarization demultiplexer is schematically shown in **Figure 4a**. In this case, we choose a slot waveguide to achieve sufficient angular separation for the slab beams excited by the fundamental TE and TM waveguide modes, respectively. The propagation angles for the beams

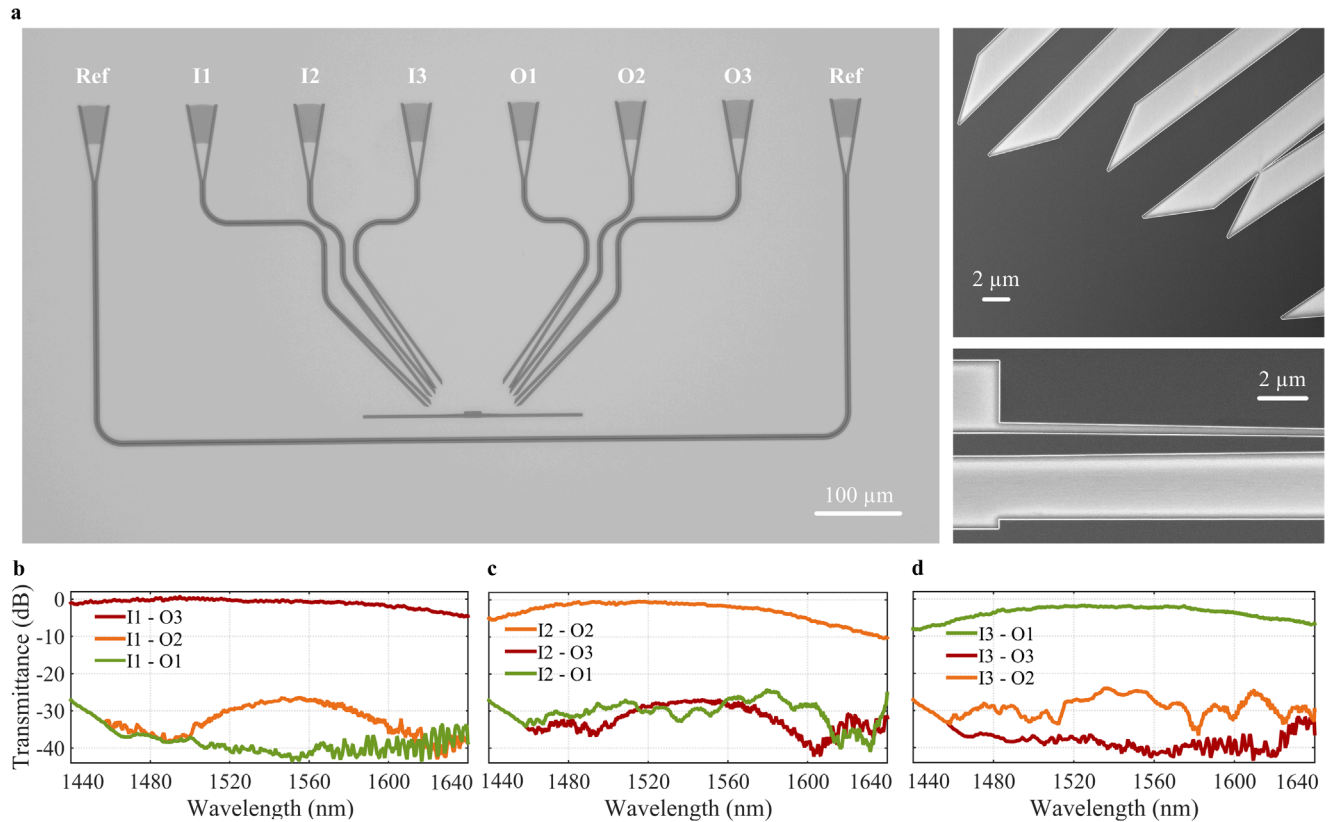


Figure 3. a) Optical and SEM images of the fabricated MDM link. Input and outputs have been numbered from left to right. The top-right inset shows details of collecting waveguides, whereas the bottom-right inset shows the taper-slab coupling region. Measured transmission spectra of the complete multiplexer-demultiplexer link for light input at b) I1, c) I2, and d) I3, which correspond to TE₀, TE₁, and TE₂ channels, respectively.

phase-matched to the TE₀ and TM₀ modes of a strip waveguide, calculated as a function of the waveguide width (W), are shown in Figure 4b. The angle difference is lower than 10°, hampering the spatial separation of the two beams. The angle at which the beams propagate within the slab is determined by the ratio n_{eff}^m/n_s , as dictated by Equation (2). Although effective indices of the TE₀ and TM₀ modes of a strip waveguide are quite different (e.g., $\Delta n_{\text{eff,TE-TM}} = n_{\text{eff,TE}}^0 - n_{\text{eff,TM}}^0 = 0.66$ for $W = 500\text{nm}$ and 1550 nm wavelength), similar propagation angles are obtained from Equation (2) as $n_{\text{eff,TE}}^0/n_{s,\text{TE}} \cong n_{\text{eff,TM}}^0/n_{s,\text{TM}} = 0.86$ (for $W = 500\text{nm}$ and 1550 nm wavelength). This limitation is overcome using a slot waveguide. We fix a slot width of $G_s = 100\text{ nm}$ and calculate the propagation angles for the TE₀ (θ_{TE}) and TM₀ (θ_{TM}) modes of the slot waveguide as a function of the rail width, W_R (see Figure 4c). For the input waveguide, we choose a rail width of $W_R = 350\text{ nm}$, yielding initial propagation angles of $\theta_{\text{TE}} = 50^\circ$ and $\theta_{\text{TM}} = 60^\circ$.

The rail width and the separation between the slab and the slot waveguide are linearly reduced along the coupling region to achieve a near-Gaussian profile at the focal points for the two slab beams. The optimized geometrical parameters are $G_I = 400\text{ nm}$ to $G_E = 100\text{ nm}$, $W_E = 100\text{ nm}$ and $L_T = \mu\text{m}$. 3D FDTD simulations are carried out to assess the performance of the polarization beam splitter (PBS). The fields radiated into the slab have an MFD of $3.5\ \mu\text{m}$ for TE₀ input and $3.8\ \mu\text{m}$ for TM₀ input.

The simulated transfer function for each polarization is shown in Figure 4d,e. Insertion losses are as low as 0.26 dB for the TE₀ mode and 0.15 dB for the TM₀ mode at the central wavelength. Crosstalk is -61.9 and -47.9 dB at the same wavelength when TE₀ and TM₀ modes are injected, respectively. Notably, the crosstalk is below -37.4 dB within the simulated bandwidth.

3.2. Fabrication and Experimental Characterization of the PDM Link

We fabricated a complete PDM link comprising two PBSs connected in a back-to-back configuration through a $10\text{-}\mu\text{m}$ -long slot waveguide, using the same SOI wafers and fabrication methods described in Section 2.3. Optical and SEM images of the fabricated devices are shown in Figure 5a. Two PDM links with nominally identical dimensions for the multiplexers and different grating couplers were fabricated to characterize losses and crosstalk, respectively. The PDM link used for loss characterization has grating couplers optimized for TE polarization for input I2 and output O1 and grating couplers optimized for TM polarization for input I1 and output O2. The PDM link used for crosstalk characterization has TE grating couplers for input I2 and output O2 and TM grating couplers for input I1 and output O1. TE and TM grating couplers have similar radiation angles. Each link includes

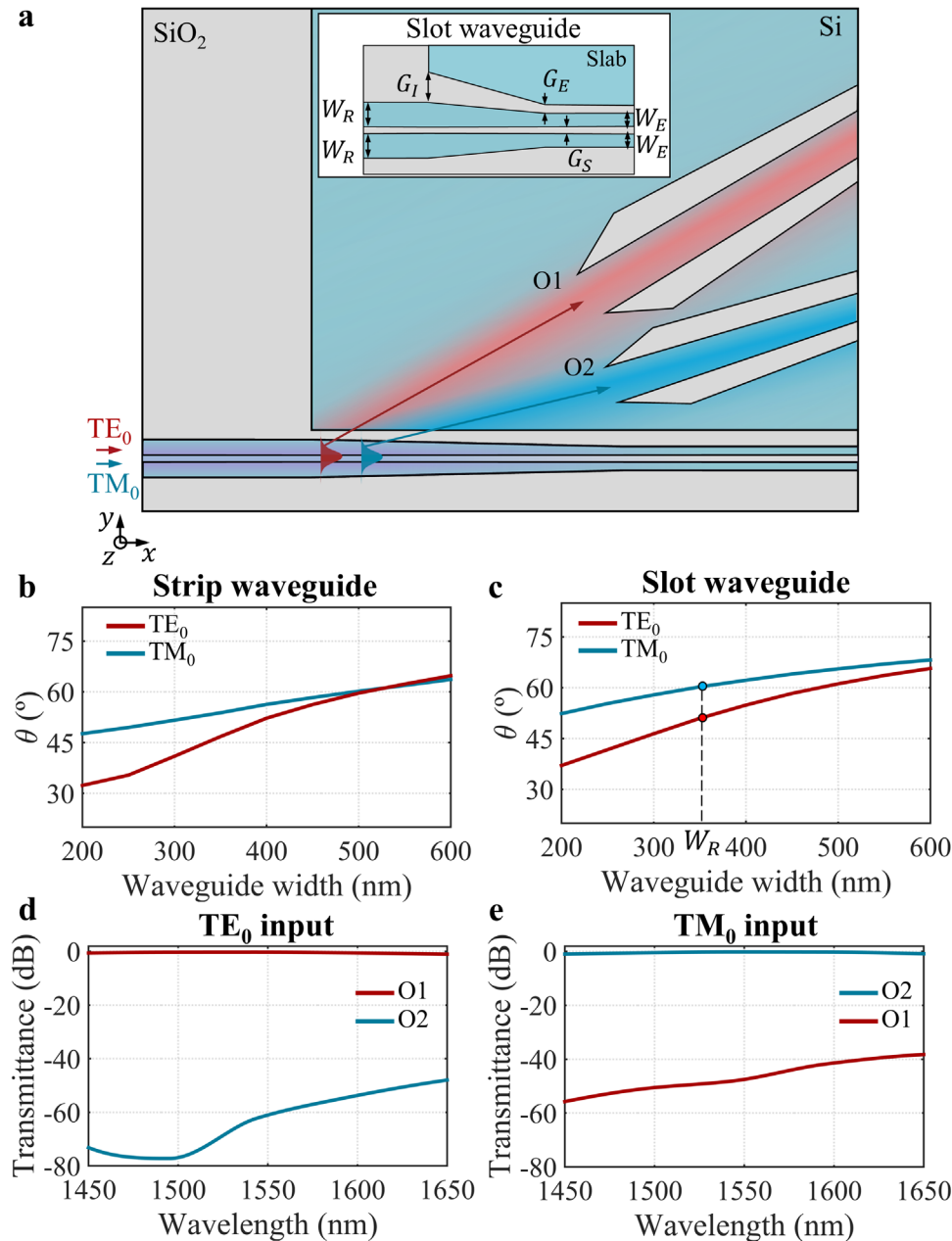


Figure 4. a) Schematic top view of the proposed two-polarization demultiplexer comprising a tapered slot waveguide and an adjacent slab. The PMMA cladding is not shown for clarity. The inset shows the geometry of the slot waveguide. Propagation angle within the slab of TE₀ and TM₀ modes as a function of the waveguide width for b) a strip waveguide and c) a slot waveguide, calculated for a Si thickness of 220 nm at $\lambda_0 = 1550$ nm. The simulated transmittance to each of the output as a function of the wavelength when d) TE₀ and e) TM₀ are launched into the slot nanowire.

two reference waveguides on the outermost part to perform the alignment and transmittance normalization for both TE and TM polarizations.

The transmittance of the link is characterized using the experimental setup described in Section S3, Supporting Information. Measured peak insertion losses are as low as 0.5 dB with a 1-dB bandwidth exceeding 100 nm and crosstalk of -40.1 dB for TE₀, and as low as 0.7 dB with a 1-dB bandwidth exceeding 108 nm and a crosstalk of -46.7 dB for TM₀. The red spectral shift is attributed to fabrication imperfections, in good agreement with

under-etching errors margins (see Section S2, Supporting Information). Ultra-low inter-modal crosstalk of -35 dB is attained for both polarizations within the measured 180 nm bandwidth. Crosstalk reaching values below -40 dB could be observed in the 1542–1680 nm wavelength range for the TM₀ channel.

4. High-Speed Data Transmission

We have characterized the quality of the multiplexing and demultiplexing realized by the three-mode and two-polarization links in

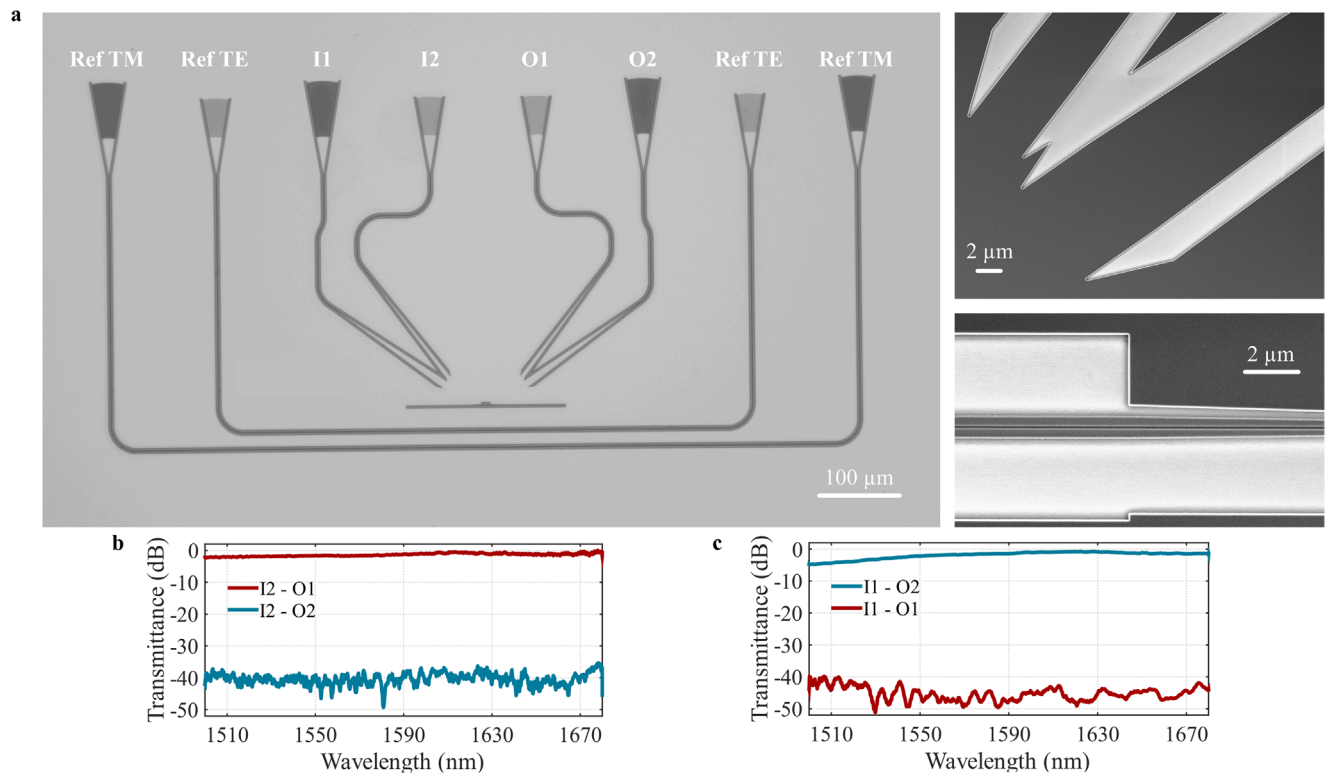


Figure 5. a) Optical and SEM images of one of the fabricated PDM links. Input and outputs have been numbered from left to right. The top-right inset shows details of collecting output waveguides, whereas the bottom-right inset shows the slot-slab coupling region. Measured transmission spectra of the complete multiplexer-demultiplexer link for light input at b) I2 and c) I1, which correspond to TE₀ and TM₀ channels, respectively.

terms of BER. The experimental setup employed is described in Section S3, Supporting Information. The figure of merit used to quantify the dynamic performance is the power penalty, defined as the difference of the minimum optical powers measured in front of the fibered receiver with and without signal impairment (i.e., crosstalk), to achieve error-free transmission (BER 10^{-9}) without using any correction technique. **Figure 6** shows the evolution of the BER as a function of the average received power for the reference, single-port transmission, and MDM and PDM operation. For the MDM link, the worst case occurs when all three signals are introduced simultaneously due to the crosstalk of the aggressor channels. Still, the power penalties are as low as 0.5, 1.5, and 0.6 dB for TE₀, TE₁, and TE₂ mode channels, respectively. As expected from static measurements, the highest power penalty is obtained for TE₁ mode channel since the cumulative crosstalk of the aggressor channels towards this other channel is higher (see Figure 3b,d, orange curves). The PDM link, on the other hand exhibits negligible crosstalk penalties for both TE₀ (0.08 dB) and TM₀ (0.03 dB) channels. Power difference between reference (Ref) and single-port (w/o XT) measurements are 0 dB (TE₀ channel), 0.04 dB (TE₁ channel), and 0.06 dB (TE₂ channel) for the MDM link, and 0.25 dB (TE₀ channel) and 0.19 dB (TM₀ channel) for the PDM link. In all cases, the demultiplexed signals exhibit clear and open eye diagrams indicating a low effective crosstalk, as shown in the insets of Figure 6. These results indicate that the proposed devices have an excellent potential for data transmission in next-generation MDM and PDM communication systems.

5. Discussion and Conclusions

In conclusion, we have shown a new approach for spatial and polarization multiplexing, exploiting the excitation of optical beams free propagating in the chip plane to achieve state-of-the-art performance. To demonstrate the concept, we have developed a three-mode and a two-polarization links allowing error-free propagation of 40 Gbps signals with low or negligible power penalties. The three-mode link takes advantage of the strong modal dispersion in strip waveguides to realize mode multiplexing and conversion based on free-space-like optical beam forming on chip. The proposed three-mode link comprising a multiplexer and a demultiplexer shows a measured crosstalk lower than -20 dB over a 195 nm bandwidth (1443–1638 nm) that fully covers the S, C, and L telecommunication bands, and partially covers the E and U bands. Furthermore, insertion losses of a single (de)multiplexer are lower than 1.5 dB over a 92 nm bandwidth considering all three modes. The two-polarization link harnesses birefringence engineering in slot waveguides to yield an ultra-low crosstalk below -35 dB within the 1500–1680 nm wavelength range for both polarizations (covering the entire C, L, and U bands, and part of the S band). Measurements also showed that insertion losses of a single PBS are below 1.5 dB for TE₀ and TM₀ within a broad bandwidth exceeding 147 nm, limited at the upper bound by the wavelength range of the laser available in our setup.

The low crosstalk values (-40 dB) observed in the MDM link for TE₀ and TE₂ modes suggest that increasing the separation of the focal points within the slab is a simple but effective way

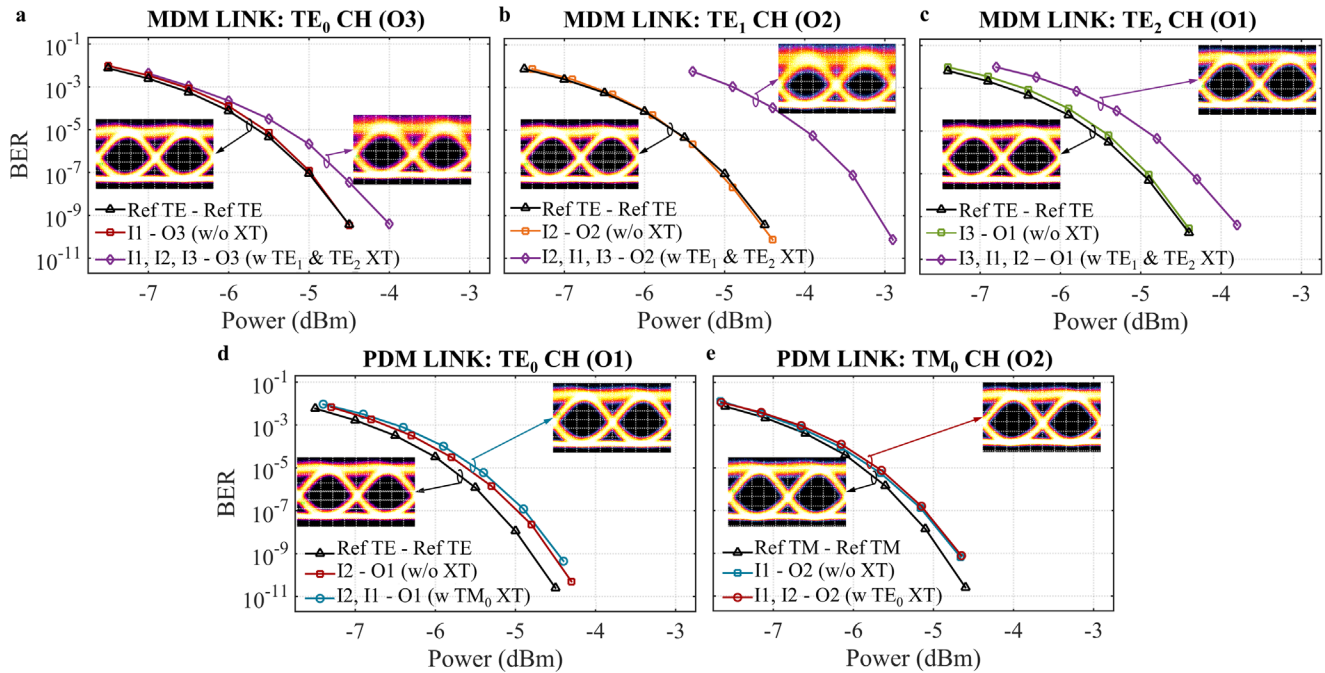


Figure 6. Crosstalk penalty assessment of MDM and PDM links for a transmission bit rate of 40 Gbps at 1549 nm. BER measurements as a function of the received power for a) TE₀ channel, b) TE₁ channel and c) TE₂ channel of the MDM link, and for d) TE₀ channel and e) TM₀ channel of the PDM link. The insets show the corresponding eye diagrams of the demultiplexed output signals (x-axis: 5 ps/div and y-axis: 0.5 mW per div). Ref, Reference link; XT, Crosstalk signal(s); CH, Channel signal.

Table 1. Comparison of demonstrated state-of-the-art three-channel MDM links and PBS using 220-nm-thick silicon core.

MDM/PBS	Ref.	Architecture	IL [dB]	BW _{XT-20 dB} [nm]	BW _{XT-30 dB} [nm]	S [μm × μm]
MDM	[7]	Asymmetric Y-junction	1.5 ~ 4.5*	–	–	320 × 6.1
	[9]	Counter-tapered coupler	6.5 ~ 8*	–	–	260 × 4.4
	[10]	Adiabatic coupler	<0.2	65	–	310 × 3.84
	[11]	Subwavelength asymmetric Y-junction	<1*	≈50*	–	4.8 × 3.6
	[12]	Subwavelength DC	<3*	–	–	88 × 20
	This work		In-slab beamforming	0.3 ~ 1.7	195	–
PBS	[14]	MMI	≈1.2	–	–	132.64 × 4.2
	[15]	MZI	≈10	≈20*	–	340 × 60
	[16]	DC	<0.5	125	–	97.4 × 3.5
	[17]	Asymmetric DC	–	–	–	25.5 × 4.8*
	[18]	Counter-tapered coupler	<0.1	15*	–	5 × 1.15
	[19]	Bent DC	<0.1	135	70	20 × 6.9
	[20]	Cascaded triple bent DC	0.2	90	≈50*	≈26 × 12
	[21]	MMI with photonic crystal	0.68 ~ 0.81	77	–	71.5 × 3.9
	[22]	Slot asymmetric DC	–	–	–	>13.6 × 1.27
	[23]	Subwavelength MMI	0.28 ~ 0.49	–	–	92.7 × 4
	[24]	Subwavelength meta-prism	0.6 ~ 1.1*	>415	–	15 × 7
[25]	Tilted-nanogratings	<0.5*	–	–	>6.8 × 1.22	
[26]	Extreme skin-depth DC	<0.6	30	–	14.5 × 2.45	
This work		In-slab beamforming	0.3 ~ 0.4	>180	>180	20 × 33

^{a)} Values marked with an asterisk correspond to values estimated from figures. IL, Insertion Loss at the optimum wavelength; XT, Crosstalk; BW_{XT-XX dB}, Bandwidth for which the crosstalk is less than -XX dB; S, Size of a single device.

to reduce crosstalk. This could be achieved by increasing the taper length to increase the focal length or by bending the coupling region. On the other hand, insertion losses of higher-order modes could be further reduced by improving the overlap between the modes coupled to the slab free-propagation region and the Gaussian-like profile of the collecting output waveguide modes, for example by implementing a nonlinear taper in the coupling region. Nevertheless, the proposed devices are, to the best of our knowledge, among the mode multiplexers and PBSs with the lowest measured crosstalk within an ultra-broad bandwidth. For the sake of comparison, **Table 1** shows the performance of demonstrated state-of-the-art three-channel MDM links and PBSs. Note that state-of-the-art PBSs have been usually measured in standalone configuration, therefore, we have halved the insertion losses measured by our PDM link to ensure a fair comparison.

A high-speed optical communications demonstration was also performed to illustrate the applicability of the proposed devices. System-level experiments at 40 Gbps without forward error correction were conducted for both MDM and PDM links, showing clear and open eye diagrams during the joint transmission of data channels. BER measurements further validated the good transmission capabilities with less than a 1.5 dB power penalty for the MDM link and below 0.08 dB for the PDM link. The ease of scalability of the proposed architecture along with such low penalties can be exploited to implement hybrid WDM-PDM-MDM optical links to significantly enhance the transmission capacity.

The strategy demonstrated here could seamlessly be extended for a larger number of modes and simultaneous modal and polarization multiplexing. Scaling the number of MDM channels would require increasing the total device size to accommodate the collecting waveguides. Parabolic tapers could be used to reduce the width of the collecting waveguides, thus the total device size. A combination of MDM and PDM could be realized by employing multimode slot waveguides. The low crosstalk, wide bandwidth, and versatility of the proposed multiplexing approach presented in this work should also open up unique possibilities in quantum information sciences, optical sensing, on-chip wireless communications, and nonlinear photonics.

Supporting Information

Supporting Information is available from the Wiley Online Library or from the author.

Acknowledgements

This work was funded by the French Industry Ministry (Nano2022 project under IPCEI program); the Agence Nationale de la Recherche (ANR-MIRSPEC-17-CE09-0041, ANR-KASHMIR-22-CE24-0021, ANR-BRIGHT-18-CE24-0023-01); the European Union's Horizon Europe (Marie Skłodowska-Curie grant agreement No. 101062518). This work was done within the C2N micro nanotechnologies platforms and partly supported by the RENATECH network and the General Council of Essonne.

Conflict of Interest

The authors declare no conflict of interest.

Data Availability Statement

The data that support the findings of this study are openly available at Zenodo repository: <https://doi.org/10.5281/zenodo.8051291>.

Keywords

integrated optics, optical beam forming, polarization division multiplexing, silicon photonics, slab, spatial division multiplexing

Received: April 3, 2023

Revised: June 9, 2023

Published online:

- [1] S. Bernabé, Q. Wilmart, K. Hasharoni, K. Hassan, Y. Thonnart, P. Tissier, Y. Désières, S. Olivier, T. Tekin, B. Szelag, *Solid State Electron.* **2021**, 179, 107928.
- [2] S. Rumley, M. Bahadori, R. Polster, S. D. Hammond, D. M. Calhoun, K. Wen, A. Rodrigues, K. Bergman, *Parallel Comput.* **2017**, 64, 65.
- [3] P. J. Winzer, D. T. Neilson, A. R. Chraplyvy, *Opt. Express* **2018**, 26, 24190.
- [4] H. Yu, D. Patel, W. Liu, Y. Malinge, P. Doussiere, W. Lin, S. Gupta, K. Narayanan, I. Hoshino, M. Bresnehan, S. Sunkoju, D. Mategazza, R. Herrick, R. Venables, H. Mahalingam, P. Seddighian, A. Fuerst, J. Davis, D. Gold, X. Pan, K. Al-hemyary, A. Agrawal, Y. Li, X. Zheng, M. Geethachar, M. Favaro, D. Zhu, A. Liu, Y. Akulova, presented at 2022 OFC, San Diego, United States, **2022**, 6–10.
- [5] D. Dai, J. E. Bowers, *Nanophotonics* **2014**, 3, 283.
- [6] D. González-Andrade, A. Dias, J. G. Wangüemert-Pérez, A. Ortega-Moñux, Í. Molina-Fernández, R. Halir, P. Cheben, A. V. Velasco, *Opt. Laser Technol.* **2020**, 129, 106297.
- [7] W. Chen, P. Wang, T. Yang, G. Wang, T. Dai, Y. Zhang, L. Zhou, X. Jiang, J. Yang, *Opt. Lett.* **2016**, 41, 2851.
- [8] D. Dai, J. Wang, Y. Shi, *Opt. Lett.* **2013**, 38, 1422.
- [9] J. Wang, Y. Xuan, M. Qi, H. Huang, Y. Li, M. Li, X. Chen, Z. Sheng, A. Wu, W. Li, X. Wang, S. Zou, F. Gan, *Opt. Lett.* **2015**, 40, 1956.
- [10] C. Li, D. Dai, *Opt. Lett.* **2017**, 42, 2370.
- [11] W. Chang, L. Lu, X. Ren, D. Li, Z. Pan, M. Cheng, D. Liu, M. Zhang, *Opt. Express* **2018**, 26, 8162.
- [12] Y. He, Y. Zhang, X. Jiang, C. Qiu, Y. Su, presented at 2017 ECOC, Gothenburg, Sweden, **2017**, 17–21.
- [13] D. González-Andrade, R. Fernández de Cabo, J. Vilas, I. Olivares, A. Dias, J. M. Luque-González, J. G. Wangüemert-Pérez, A. Ortega-Moñux, Í. Molina-Fernández, R. Halir, P. Cheben, A. V. Velasco, *IEEE Photonics Technol. Lett.* **2021**, 33, 1262.
- [14] M. Yin, W. Yang, Y. Li, X. Wang, H. Li, *Opt. Commun.* **2015**, 335, 48.
- [15] K. Morita, H. Uenohara, *IEEE Photonics J* **2018**, 10, 6600908.
- [16] Z. Lu, Y. Wang, F. Zhang, N. A. F. Jaeger, L. Chrostowski, *Opt. Lett.* **2015**, 23, 29413.
- [17] J. Wang, D. Dai, presented at 2013 OFC, Anaheim, United States, **2013**, 17–21.
- [18] W. Chen, B. Zhang, P. Wang, S. Dai, W. Liang, H. Li, Q. Fu, J. Li, Y. Li, T. Dai, H. Yu, J. Yang, *Opt. Express* **2020**, 28, 30701.
- [19] H. Wu, Y. Tan, D. Dai, *Opt. Express* **2017**, 25, 6069.
- [20] J. R. Ong, T. Y. L. Ang, E. Sahin, B. Pawlina, G. F. R. Chen, D. T. H. Tan, S. T. Lim, C. E. Png, *Opt. Lett.* **2017**, 42, 4450.
- [21] L. Xu, Y. Wang, E. El-Fiky, D. Mao, A. Kumar, Z. Xing, M. G. Saber, M. Jacques, D. V. Plant, *J Lightwave Technol* **2019**, 37, 1231.
- [22] S. Lin, J. Hu, K. B. Crozier, *Appl. Phys. Lett.* **2011**, 98, 151101.

- [23] L. Xu, Y. Wang, A. Kumar, D. Patel, E. El-Fiky, Z. Xing, R. Li, D. V. Plant, *IEEE Photonics Technol. Lett.* **2018**, *30*, 403.
- [24] H. Xu, Y. Qin, G. Hu, H. K. Tsang, *Laser Photonics Rev.* **2023**, 2200550.
- [25] H. Liu, J. Feng, J. Ge, S. Zhuang, S. Yuan, Y. Chen, X. Li, Q. Tan, Q. Yu, H. Zeng, *Nanomaterials* **2021**, *11*, 2645.
- [26] S. Z. Ahmed, I. Ahmed, M. B. Mia, N. Jaidye, S. Kim, *Opt. Lett.* **2021**, *46*, 2164.
- [27] H. Xu, D. Dai, Y. Shi, *Laser Photonics Rev.* **2019**, *13*, 1800349.
- [28] C. Williams, G. Zhang, R. Priti, G. Cowan, O. Liboiron-Ladouceur, *Opt. Express* **2019**, *27*, 27712.
- [29] H. M. Stoll, *Appl. Opt.* **1978**, *17*, 2562.
- [30] P. J. Bock, P. Cheben, A. Delâge, J. H. Schmid, D.-X. Xu, S. Janz, T. J. Hall, *Opt. Express* **2008**, *16*, 17616.
- [31] P. Cheben, P. J. Bock, J. H. Schmid, J. Lapointe, S. Janz, D.-X. Xu, A. Densmore, A. Delâge, B. Lamontagne, T. J. Hall, *Opt. Lett.* **2010**, *35*, 2526.
- [32] P. J. Bock, P. Cheben, J. H. Schmid, A. V. Velasco, A. Delâge, S. Janz, D.-X. Xu, J. Lapointe, T. J. Hall, M. L. Calvo, *Opt. Express* **2012**, *20*, 19882.
- [33] A. Hadij-ElHouati, A. Ortega-Moñux, J. G. Wangüemert-Pérez, R. Halir, S. Wang, J. H. Schmid, P. Cheben, I. Molina-Fernández, *Opt. Lett.* **2021**, *46*, 4821.
- [34] S. Kim, D. A. Westly, B. J. Roxworthy, Q. Li, A. Yulaev, K. Srinivasan, V. A. Aksyuk, *Light Sci Appl* **2018**, *7*, 72.
- [35] C. Ropp, A. Yulaev, D. Westly, G. Simelgor, V. Aksyuk, *Opt. Express* **2021**, *29*, 14789.
- [36] D. Headlad, W. Withayachumnankul, M. Fujita, T. Nagatsuma, *Optica* **2021**, *8*, 621.
- [37] T. Tamir, S. T. Peng, *Appl. Phys.* **1977**, *14*, 235.
- [38] A. Sánchez-Postigo, J. G. Wangüemert-Pérez, J. M. Luque-González, Í. Molina-Fernández, P. Cheben, C. Alonso-Ramos, R. Halir, J. H. Schmid, A. Ortega-Moñux, *Opt. Lett.* **2016**, *41*, 3013.